An IB-LBM investigation into the aerodynamic coefficients in relation to the rotation intensity of a tornado-like wind

Xixiong Guo, Jun Cao *

Department of Mechanical and Industrial Engineering, Ryerson University, Toronto, Ontario, Canada, M5B 2K3

A B S T R A C T

A tornadic wind is essentially considered as an airflow that simultaneously translates and rotates. Numerical simulations of this kind of hybrid flow remain inadequate due to many numerical difficulties, one of the major challenges consisting in the establishment of a set of boundary conditions that are, for the tornado–obstacle interaction scenario, both rational in physics and simple in numerical implementation. Inspired by the success of immersed-boundary (IB) lattice Boltzmann method (LBM) for simulations of fluid–structure interaction problems, this study proposes a new outlet of the IB-LBM framework for investigation of tornadic wind effects, featuring a reformed interpretation of the Rankine-Combined Vortex Model (RCVM) that considerably facilitates the boundary condition setup. Moreover, the main purpose of this study is to examine the tornadic wind loadings in relation to the rotation intensity of a tornado, and presents a practical Newton's bi-section-like method for determining the critical rotation intensity beyond which the aerodynamic coefficients no longer increase when Reynolds number rises. This critical rotation intensity serves to characterize tornadic winds, such that the tornado with a rotation density below its critical value can be considered as mainly dominated by the translation part and, otherwise, the dominance no longer belongs only to the translational component of the tornado. Since it has been rather conventional that, when studying tornadoes, Reynolds number is determined using only the translation velocity as characteristic velocity, the present tornado study intends to suggest, through a number of numerical test series, that more attention be paid to the insufficiently explored rotational component, which physically tends to play a more dominant role when an intensive rotation is present in a tornado scenario.

1. Introduction

As meteorological disaster, a tornado may induce a significantly elevated level of wind forces if compared to a straight-line wind, and cause severe property damages. The tornado dynamics has been experimentally studied. For example, Ward [1] first developed a tornado simulator with a fan at the top to generate updraft flow. This simulator could be used to only study purely rotational flow without any translation component involved, which was inadequate to simulate a real-world tornado. Then, modifications have been made by other researchers [2–4] aimed at enabling the simulator to generate more realistic tornado scenarios.

Due to the obvious drawback in using laboratorial simulator, including long set-up time, considerable expense, and other restrictive conditions, more efforts are nowadays made by the tornado research community in mathematical modeling and

---

  * Corresponding author.
    E-mail address: jcao@ryerson.ca (J. Cao).

numerical simulation of the tornado phenomena. Obviously, a properly designed model for a straight-line wind would fail to describe a tornado-like wind even if the two winds have the same translational speed [5]. This is because a tornado can be essentially decomposed into simultaneous translational and rotational flow components, and both have to be considered in the model for a tornado. A well established tornado model has always been sought, since it would help the researchers better understand, through economical computer-aided simulations, the tornado dynamics as well as the mechanism of tornado–building interaction and, ultimately, improve the design of buildings towards their enhanced wind-resistant capabilities.

Over the past few decades, Wilson [6] first applied a two dimensional tornado model to examine the effects of tornadoes on rectangular-shaped buildings. Nolan and Farrell [7] used the axisymmetric Navier–Stokes (N–S) equations with a constant viscosity to explore the structure and dynamics of tornado-like vortices. Lewellen et al. [8,9] employed a three-dimensional large eddy simulation (LES) turbulence model to investigate the dynamics of a tornado-like vortex near the surface with particular attention paid to the turbulent flow characteristics in the corner region. Ishihara et al. [10] developed a tornado model by incorporating LES in the time-dependent N–S equations to simulate the flow fields of one-celled and two-celled vortices.

On the other hand, tornado-induced wind loads exerted on constructions have been also a practical numerical simulation topic. However, very little literature can be found that numerically investigated the tornadic wind loadings on buildings. Two representative pieces of work in this regard are inspirational to the present study. The numerical simulations performed by Selvam et al. [11–13] employed the Rankine-combined Vortex Model (RCVM) with focus placed on the tornado–building interaction. They reported the tornado-induced loads on 2D sections of a cylinder and multi-cubic buildings using the finite difference discretization of the N–S equations [11,12], with further extensions to 3D cases [13] at elevated Reynolds numbers with the aid of LES model [14]. Also, Bienkiewicz and Dudhia [15] conducted comparative studies to examine the wind loads and surface pressure on small building models in the cases of swirling, tornado-like, and straight-line winds, finding that the loadings induced by the swirling and tornado-like winds are significantly higher (3 to 5 times) than in the case of a straight-line wind, and the surface pressure distributions are also quite different between each other.

An important remark made by [15] for the tornado research community is that the effect of a tornadic wind is of strongly hybrid nature since both translational and rotational airflow components take part in a tornado scenario, thus, reliance on the translation part of a tornado for establishment of tornado research framework, such as employing the translation velocity component for determining the Reynolds number of a tornado and then using such a translational speed based Reynolds number to characterize tornadoes, tends to make little sense once the rotation part of a tornado is intensive enough to overcome the dominance of the translational component. However, further investigation into the influence of the rotational part to the overall tornado wind loading effects is so far found very rare in existing literature. Without sufficient examination about the impact of the rotational component in a tornado, the understanding of the tornado dynamics and the tornado–building interaction mechanism may remain incomplete or even inaccurate, and skewed perspective might result from the tornado framework built excessively upon the translational part but defectively upon the rotational part. In order to acquire a better comprehension about the tornadic wind induced loads on a civil construction, this study aims to place a particular probe, through numerical simulations with the aid of RCVM-based tornado model, into the relation between the aerodynamic coefficients and the rotational component of a tornadic wind.

The aforementioned tornado simulations [8–12,15] mainly relied on conventional numerical methods to build their N–S based solvers. When solving the N–S equations, the obviously time-variant boundary conditions of the tornado-like flow field have to be updated for every time step. Different from the reported tornado solvers, the present study proposes a novel lattice Boltzmann method (LBM) based computational framework with the immersed boundary (IB) approach properly embedded, such that the tedious updating process for prescribing the boundary conditions of tornado simulation domain can be successfully circumvented.

In fact, as an alternative to the Navier–Stokes equations based solver, LBM [16] has been often used for simulating viscous flow in recent years due to its noticeable advantages in terms of simplicity for implementation, parallelizability for algorithmic development, and robustness for applications [17,18]. On the other hand, the IB method proposed by Peskin [19,20] is an attractive approach when a moving boundary problem is dealt with. As a non-boundary conforming approach, IB introduces an additional "restoring" force in the vicinity of a moving object that is immersed in a fluid, so that all the effects of the fluid to the boundary of the solid object can be taken into account and, then, this additional force is distributed back to the affected grid nodes to form a special body force. In 2004, the IB scheme was successfully incorporated in LBM by Feng and Michaelides [21]. They demonstrated the remarkable advantage of IB-LBM when simulating 2D and 3D particulate flows [22]. Lately, considerable IB-LBM progress has been achieved in solving challenging fluid–solid interaction (FSI) problems, such as biomimetic simulation focusing on flapping/flexible foil [23,24] and the flapping of multiple elastic structures [25], particulate–fluid interaction flow [26], solid–liquid phase change problems [27].

Inspired by the reported IB-LBM application success [21–27], this study aims to numerically open a novel IB-LBM outlet for simulation of tornado–building interaction. As the tornado-like wind can be decomposed into two components, namely, rotation and translation, the scenario of a tornado towards a building is re-interpreted, in this study, as a "*virtual*" translation of the building towards a rotating airflow about its "*virtually locked*" center, which implies the application of the "*relative motion*" principle to the translation component of the tornadic wind; then, the IB approach is employed to mathematically model the "*virtually moving*" building. This novel interpretation for the tornado–building interaction greatly facilitates the boundary condition set up. That is, the outer boundary of the tornadic wind domain can be prescribed by simply using the

rotation part of the tornado according to RCVM, while the satisfaction of the no-slip boundary condition for the building can be guaranteed by the IB model. Guided by this novel interpretation, under numerical investigation in this study are a number of test series for tornado-like flows with different rotation intensities that pass over an obstacle, and a detailed study will be conducted that focuses on the impact of the rotation intensity to the overall tornado-induced forces.

The rest of this paper will unfold as follows. The tornadic wind model, referred to as Rankine-combined Vortex Model (RCVM), along with its re-tailored version is presented in Section 2. Section 3 describes the IB-LBM framework that is employed in this tornado simulation study, followed by Section 4 in which the present IB-LBM based tornado model is validated using separated translational and rotational flow cases. In Section 5, a number of test series corresponding to tornadic flows over a cylinder are examined with focus particularly placed on the effects of the rotation intensity to the overall wind loadings exerted on the obstacle. Finally, concluding remarks are made in Section 6, emphasizing the necessity of further exploring the rotational component of tornado in order to gain a more complete comprehension about the tornado dynamics as well as, for more practical reason, the tornado–building interaction mechanism.

2. Tornado-like flow model

2.1. Rankine-combined vortex model (RCVM)

The Rankine-combined vortex model (RCVM) featuring inherently satisfying the Navier–Stokes equation [11] while exhibiting a simple analytic form is pertinent for describing a tornado-like wind over a two-dimensional obstacle-free domain. The RCVM velocity profile can be decomposed into a constant translation component, $\vec{V}_t$, and a component of rotation with respect to the wind center, $\vec{V}_\theta$, which denotes the tangential velocity within the circular-motion context. According to RCVM, V_θ varies with the distance from the vortex center, r. Let r_c represent the critical radius where the peak tangential velocity, $(V_\theta)_{max}$, takes place. When $r \leq r_c$, $V_\theta = r\omega$ indicates the tangential velocity increases linearly with r at a constant angular velocity ω; when $r > r_c$, $V_\theta = r_c^2\omega/r$ shows the tangential velocity decreases right after the presence of $(V_\theta)_{max}$. The expressions can be summarized as:

$$V_\theta = \begin{cases} r\omega, & r \leq r_c \\ r_c^2\omega/r, & r > r_c. \end{cases} \tag{1}$$

When an obstacle is present in a tornadic wind field, the idealized RCVM is no longer applicable to the entire flow domain due to the wind–obstacle interaction. In practice, RCVM still can serve to initialize the flow domain, physically representing a tornadic wind that has not been affected by the obstacle provided the wind center and the obstacle are distant from each other at the beginning. Remark that real tornado scenario unfolds with an identical translational velocity, $\vec{V}_t = V_{tx}\vec{i} + V_{ty}\vec{j}$, applicable to the whole flow domain while the building remains immobile, in addition to the rotation about the moving wind center. In the light of RCVM, at a given time instant, t, the resultant velocity at a point (x, y) located in the counterclockwisely-rotating tornado field reads:

$$\vec{V} = \vec{V}_t + \vec{V}_\theta = (V_{tx} - V_\theta \sin\theta)\vec{i} + (V_{ty} + V_\theta \cos\theta)\vec{j} \tag{2}$$

with

$$\theta = \tan^{-1}\left(\frac{y - y_c(t)}{x - x_c(t)}\right) \tag{3}$$

where $x_c(t) = x_{c0} + v_{tx}t$ and $y_c(t) = y_{c0} + v_{ty}t$ with (x_{c0}, y_{c0}) denoting the initial position of the tornado center, and θ stands for the angle between the radial line passing through (x, y) and the horizontal direction pointing to the right. Clearly, in RCVM, $\theta = \theta(x, y, t)$ and, in turn, $\vec{V} = \vec{V}(x, y, t)$.

2.2. Re-tailored RCVM

Due to the translation of the tornado center, the resultant velocity in RCVM eventually turns out to be $\vec{V} = \vec{V}(x, y, t)$. In this sense, if attempting to employ RCVM for prescription of the boundary condition, updating the boundary condition becomes mandatory due to its time-dependent nature, which poses computational complexity if purely relying on conventional Computational Fluid Dynamics (CFD) methods without any modification.

This tornado modeling study intends to re-tailor the original RCVM such that the boundary condition of a tornadic wind domain with presence of an obstacle can be established still on the basis of RCVM but in a time-independent form. That is, by using the concept of "*relative motion*", the translation part of RCVM is detached from the tornado center, and now attached to the obstructed building, such that the tornado center is "*pinned*", i.e., $x_c(t) \equiv x_{c0}$, $y_c(t) \equiv y_{c0}$, while the building is viewed as "*in motion*" with a velocity that is equal to the original translation magnitude but opposite to the real tornado translation direction. Consequently, the interaction scenario between the tornado and the building is described as the building "*virtually entering*", at a translational velocity $\vec{V}_t = -(V_{tx}\vec{i} + V_{ty}\vec{j})$, a purely rotational airflow $\vec{V}_\theta = V_\theta(-\vec{i}\sin\theta + \vec{j}\cos\theta)$ in which $\theta = \tan^{-1}\left(\frac{y - y_{c0}}{x - x_{c0}}\right)$ becomes no longer related to the time, t. This new interpretation (Fig. 1) facilitates setting the boundary
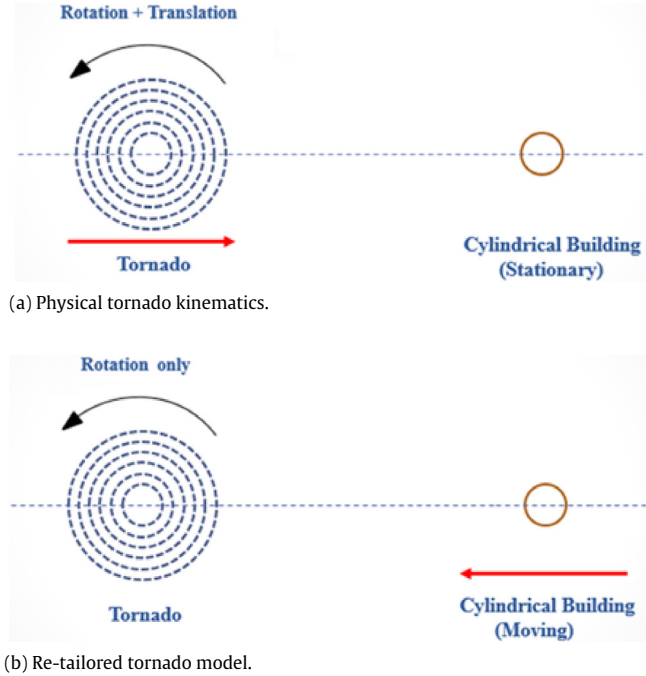
(a) Physical tornado kinematics.

(b) Re-tailored tornado model.

Fig. 1. Physical and re-tailored RCVM.

condition for the outer boundary of the tornado domain under numerical simulation, which turns out to be only the aforementioned $\vec{V}_\theta$ that requests no updating with the elapsing time, t, after the translation part of the tornado is associated with the building. The "*virtual translation*" of the building resulting from the present re-interpreted RCVM can be modeled by the immersed boundary (IB) approach, which will be elucidated in Section 3.2. The boundary conditions afforded by this re-tailored RCVM appear both physically compatible with the flow nature and numerically much more maneuverable.

2.3. Rotation intensity in tornadic flow

The focus of this study is placed on the investigation of the impact of intensity of the rotation component in a tornado-like flow, which is denoted by β in RCVM as follows:

$$(V_\theta)_{max} = r_c\omega = \beta V_t. \tag{4}$$

Clearly, β represents the ratio of the maximum tangential flow rate of the rotational component, $(V_\theta)_{max}$, to the translational flow rate, V_t, and the larger the β, the more remarkable the dominancy of the rotation component in the overall tornadic flow. Detailed numerical experiments will be presented in Section 5, addressing the influence of rotation intensity to the aerodynamic loadings induced by a number of the tornado-like wind cases.

3. Numerical method

3.1. Lattice Boltzmann model with multiple-relaxation time collision

The flow of a viscous incompressible fluid can be numerically simulated using the multiple-relaxation-time (MRT) lattice Boltzmann model (LBM) [28] with the flow domain discretized into uniform square cells. The typical D2Q9 scheme in LBM takes $c = \delta x/\delta t = 1$ for the lattice speed, where δx is the lattice size, and δt the time step, leading to the following lattice velocity:

$$\boldsymbol{c}_i = \begin{cases} (0, 0) & i = 0 \\ (\cos[(i-1)\pi/2], \sin[(i-1)\pi/2])c, & i = 1, 2, 3, 4 \\ (\cos[(2i-9)\pi/4], \sin[(2i-9)\pi/4])\sqrt{2}c, & i = 5, 6, 7, 8. \end{cases} \tag{5}$$

Originating from the lattice Boltzmann equation (LBE), the governing equation for MRT-LBM takes the following form:

$$\boldsymbol{f}(\boldsymbol{x} + \boldsymbol{c}_i\delta_t, t + \delta_t) - \boldsymbol{f}(\boldsymbol{x}, t) = -\boldsymbol{M}^{-1}\boldsymbol{S}[\boldsymbol{R}(\boldsymbol{x}, t) - \boldsymbol{R}^{eq}(\boldsymbol{x}, t)] \tag{6}$$

where $\boldsymbol{f}$ is the vector composed of distribution functions, $\boldsymbol{M}$ is the transformation matrix, $\boldsymbol{S}$ is the diagonal relaxation matrix, $\boldsymbol{R}$ is the moment vector, $\boldsymbol{R}^{eq}$ is the corresponding equilibrium moment vector. The detailed forms of these vectors and matrices are organized as follows:

$$\boldsymbol{f} = (f_0, f_1, f_2, f_3, f_4, f_5, f_6, f_7, f_8)^T \tag{7}$$

$$\boldsymbol{S} = diag(s_0, s_1, \ldots, s_8) = diag(0, s_e, s_\varepsilon, 0, s_q, 0, s_q, s_v, s_v) \tag{8}$$

$$\boldsymbol{R} = (\rho, e, \varepsilon, j_x, q_x, j_y, q_y, p_{xx}, p_{xy})^T \tag{9}$$

$$\boldsymbol{R}^{eq} = \rho(1, -2 + 3u^2, 1 - 3u^2, u_x, -u_x, u_y, -u_y, u_x{}^2 - u_y{}^2, u_x u_y)^T \tag{10}$$

$$\boldsymbol{M} = \begin{bmatrix} 1 & 1 & 1 & 1 & 1 & 1 & 1 & 1 & 1 \\ -4 & -1 & -1 & -1 & -1 & 2 & 2 & 2 & 2 \\ 4 & -2 & -2 & -2 & -2 & 1 & 1 & 1 & 1 \\ 0 & 1 & 0 & -1 & 0 & 1 & -1 & -1 & 1 \\ 0 & -2 & 0 & 2 & 0 & 1 & -1 & -1 & 1 \\ 0 & 0 & 1 & 0 & -1 & 1 & 1 & -1 & -1 \\ 0 & 0 & -2 & 0 & 2 & 1 & 1 & -1 & -1 \\ 0 & 1 & -1 & 1 & -1 & 0 & 0 & 0 & 0 \\ 0 & 0 & 0 & 0 & 0 & 1 & -1 & 1 & -1 \end{bmatrix}. \tag{11}$$

Note that, in the relaxation matrix, the option of $s_0 = s_3 = s_5 = 0$ is permissible, and recommended for reducing the computational cost; the relaxation rates s_v and s_ε are related to the total viscosity v and bulk viscosity ζ:

$$v = c_s{}^2 \left(\frac{1}{s_v} - \frac{1}{2} \right) \delta t \tag{12}$$

$$\zeta = c_s{}^2 \left(\frac{1}{s_\varepsilon} - \frac{1}{2} \right) \delta t. \tag{13}$$

Note also that the total viscosity, v in Eq. (12), represents only the base viscosity, also referred to as kinematic viscosity, in the laminar flow case or, in the turbulent flow case, v becomes the sum of the (base) kinematic viscosity and the eddy viscosity, v_t, which will be detailed in Section 4.

The relaxation rates s_ε, s_q, s_e can be adjusted within the interval of $(0, 2)$. The matrix $\boldsymbol{M}$ is applied to transform the distribution function $\boldsymbol{f}$ onto the moment space $\boldsymbol{R}$ such that $\boldsymbol{R} = \boldsymbol{M}\boldsymbol{f}$ and $\boldsymbol{R}^{eq} = \boldsymbol{M}\boldsymbol{f}^{eq}$. The components of the corresponding equilibrium distribution function, $\boldsymbol{f}^{eq}$, are given by:

$$f_i^{eq} = w_i \rho \left[1 + \frac{\boldsymbol{c}_i \cdot \boldsymbol{u}}{c_s^2} + \frac{(\boldsymbol{c}_i \cdot \boldsymbol{u})^2}{2c_s^4} - \frac{u^2}{2c_s^2} \right], \quad i = 0, 1, \ldots, 8 \tag{14}$$

with $w_0 = 4/9, w_1 = w_2 = w_3 = w_4 = 1/9, w_5 = w_6 = w_7 = w_8 = 1/36$, and $c_s = c/\sqrt{3}$ representing the sound speed.

The density, velocity of the fluid, and the pressure of the flow are determined as follows:

$$\rho = \sum_{i=0}^{8} f_i, \quad \boldsymbol{u} = \frac{1}{\rho} \sum_{i=0}^{8} f_i \boldsymbol{c}_i, \quad p = \rho c_s{}^2. \tag{15}$$

3.2. Incorporation of immersed boundary (IB) approach in LBM

In a fluid flow problem, the interaction between the fluid and an immersed solid object can be considered as an additional forcing term, such that the computational domain becomes also inclusive of the region occupied by the solid object. This computational strategy is often referred to as immersed boundary (IB) method. When embedding the IB approach in LBM, the flow field Ω is represented by the Eulerian square lattices, which are the fixed Cartesian mesh points in the LBM framework; meanwhile, the boundary of the immersed object, which is denoted by Γ, is described by another set of points, $\boldsymbol{X}_B^l$, where the superscript l and subscript B represent the Lagrangian point and the boundary of the immersed object, respectively. Remark that this series of points is referred to as Lagrangian points because the body itself, including its boundary, is not necessarily always at rest. An external force term reflecting the fluid–solid interaction, $\boldsymbol{f}_{RST}$, which is allocated at the Eulerian points, should be numerically determined and then seamlessly added to the LBM framework. The IB and MRT-LBM incorporation are carried out through the following procedure:

Step 1: Obtain the velocity $\boldsymbol{U}_B^l$ at Lagrangian points $\boldsymbol{X}_B^l$.

For measuring the closeness of an Eulerian point, $\boldsymbol{x}_{ij} = (x_i, y_j)^t$, and a Lagrangian point, $\boldsymbol{X}_B^l = (X_B^l, Y_B^l)^t$, the following continuous kernel distribution is required:

$$D_{ij}(\boldsymbol{x}_{ij} - \boldsymbol{X}_B^l) = \delta(x_i - X_B^l)\delta(y_j - Y_B^l) \tag{16}$$

with

$$\delta(r) = \begin{cases} \dfrac{1}{4}\left(1 + \cos\left(\dfrac{\pi\,|r|}{2}\right)\right), & |r| \le 2 \\ 0, & |r| > 2 \end{cases}$$ (17)

which is proposed by Peskin [20]. Then, based on the known velocity distribution over all Eulerian points, $\boldsymbol{u} = (\boldsymbol{x}, t)$, the velocity of the fluid adhered to a Lagrangian point $\boldsymbol{X}_B^l$ can be determined by:

$$\boldsymbol{U}_B^l(\boldsymbol{X}_B^l, t) = \boldsymbol{u}(\boldsymbol{X}_B^l, t) = \sum_{i,j} \boldsymbol{u}(\boldsymbol{x}, t) D_{ij}(\boldsymbol{x}_{ij} - \boldsymbol{X}_B^l)\delta x \delta y$$ (18)

with $\delta x = \delta y = 1$ in the present LBM framework. Note Eq. (18) implies the satisfaction of no-slip condition at the boundary.

Step 2: Obtain the restoring force $\boldsymbol{F}_{RST}^l$ at Lagrangian points $\boldsymbol{X}_B^l$.

With the velocity $\boldsymbol{U}_B^l$ available at Lagrangian points, the restoring force per unit volume exerted at a Lagrangian point can be easily computed using the following feedback-forcing model [29]:

$$\boldsymbol{F}_{RST}^l = \alpha_1 \int_0^t (\boldsymbol{U}_B^l - \boldsymbol{U}_{IMS})dt + \alpha_2(\boldsymbol{U}_B^l - \boldsymbol{U}_{IMS}).$$ (19)

In Eq. (19), α_1 and α_2 are two negative free constants with dimensions of $ML^{-3}T^{-2}$ and $ML^{-3}T^{-1}$, respectively. According to [29], α_1 and α_2 are stable for moderate values within the interval $[-100, -1]$, and neither is sensitive to its exact value. $\boldsymbol{U}_{IMS}$ in Eq. (19) stands for the moving velocity of the immersed body itself. In the case of an immobile immersed body, $\boldsymbol{X}_B^l = \boldsymbol{X}_B^l(s)$, in which s denotes the Lagrangian parametric coordinate, thus, $\boldsymbol{U}_{IMS} \equiv \boldsymbol{0}$; if the immersed body moves in the fluid, then,

$$\boldsymbol{X}_B^l = \boldsymbol{X}_B^l(s, t)$$ (20)

and

$$\boldsymbol{U}_{IMS}(s, t) = \frac{\partial \boldsymbol{X}(s, t)}{\partial t}$$ (21)

which can be numerically determined using:

$$\boldsymbol{U}_{IMS}(s, t) = \frac{\boldsymbol{X}(s, t) - \boldsymbol{X}(s, t - \delta t)}{\delta t}.$$ (22)

Step 3: Obtain the restoring force $\boldsymbol{f}_{RST}$ at Eulerian points $\boldsymbol{x}_{ij}$.

The restoring force has to be expressed in the Eulerian framework, i.e., at the Cartesian grid points, so that this additional force can be seamlessly incorporated in MRT-LBM. The transformation described in Eq. (18) is now reversed for transforming $\boldsymbol{F}_{RST}^l(\boldsymbol{X}_B^l, t)$ to $\boldsymbol{f}_{RST}(\boldsymbol{x}_{ij}, t)$, resulting in

$$\boldsymbol{f}_{RST}(\boldsymbol{x}_{ij}, t) = \sum_l \boldsymbol{F}_{RST}^l(\boldsymbol{X}_B^l, t) D_{ij}(\boldsymbol{x}_{ij} - \boldsymbol{X}_B^l) \Delta s_l$$ (23)

where Δs_l is the arc length of a boundary element.

Step 4: Embed the restoring force $\boldsymbol{f}_{RST}$ in LBM.

In order to invoke $\boldsymbol{f}_{RST}$ in the LBM framework, the following transformation is employed:

$$F_i = \left(1 - \frac{1}{2\tau}\right) w_i \left(\frac{\boldsymbol{c}_i - \boldsymbol{u}}{c_s^2} + \frac{\boldsymbol{c}_i \cdot \boldsymbol{u}}{c_s^4}\boldsymbol{c}_i\right) \cdot \boldsymbol{f}_{RST}$$ (24)

with w_i representing the coefficients in the equilibrium distribution function as aforementioned for Eq. (14), such that the additional forcing term, F_i, can be included into the right hand side, leading to the following revised LBE [30]:

$$\boldsymbol{f}_i(\boldsymbol{x} + \boldsymbol{c}_i\delta_t, t + \delta_t) - \boldsymbol{f}_i(\boldsymbol{x}, t) = -\boldsymbol{M}^{-1}\boldsymbol{S}[\boldsymbol{R}_i(\boldsymbol{x}, t) - \boldsymbol{R}_i^{eq}(\boldsymbol{x}, t)] + \left(\boldsymbol{I} - \frac{\boldsymbol{S}}{2}\right)\boldsymbol{M}F_i\delta t.$$ (25)

Remark that, accordingly, the velocity in the LBM framework should also take $\boldsymbol{f}_{RST}$ into account:

$$\rho\boldsymbol{u} = \sum_{i=0}^8 f_i\boldsymbol{c}_i + \frac{1}{2}\boldsymbol{f}_{RST}\delta t.$$ (26)

4. Validation

As aforementioned, very little literature on numerical simulation of tornado-induced wind load on buildings can be found; in particular; those using RCVM as model basis are even fewer. Although the RCVM-based model developed in this study features co-existence of rotational and translational components, for the purpose of making a feasible and yet indicative comparison, a practical option is to switch one component on while turning off the other component, such that the rotational and translational flow results from the present IB-LBM approach can be at least separately compared against a variety of available relevant results [31–33].

As demonstrated in [34], the IB-LBM framework employed here owns approximately second order of accuracy, if evaluated using the method proposed in [35]. The interested readers are referred to [34] for details of accuracy validation. Also, the grid independency study conducted in [34] indicated that the results were considered grid-independent when the LBM grid resolution reaches the level of $\frac{1}{40}$.

In the present study, all IB-LBM simulations use a uniform grid ($\Delta x = \Delta y = 1$) based on Cartesian coordinates, the corresponding time step size is $\Delta t = 1$, and the relaxation time $s_1 = s_2 = s_4 = s_6 = 1.2$. In the LBM context, when defining Reynolds number, the nominal fluid density is set at $\rho = 1$, the converted translational velocity, V_t, and the cylinder diameter, $D = 1unit$, are taken as the characteristic velocity and length, respectively. In order to investigate flows with elevated Reynolds number, the Smagorinsky sub-grid stress (SGS) model [14] is incorporated in the present framework. In the SGS [14] model, an eddy viscosity ν_t is added into the total viscosity, which can be defined as:

$$\nu_t = (C_s \Delta_L)^2 \sqrt{2 \vec{S}_{ij} \vec{S}_{ij}} \tag{27}$$

where the adjustable constant C_s is the Smagorinsky constant and is fixed at 0.2 in the present study. Δ_L is the filter width. $\vec{S}_{ij}$ represents the strain rate tensor. Note that, when calculating the relaxation times in the case of a turbulent flow, ν_t should be included in the total viscosity, ν, which turns out to be the left hand side of Eq. (12).

4.1. Rotational Couette flow

The first comparison subject is a purely rotational flow, which is also referred to as rotational Couette flow. The flow domain is in a "ring" shape, which is "sandwiched" by an inner cylinder (with radius R_1) and an outer cylindrical wall (with radius R_2) that are coaxial and rotating at two different rotational velocities, Ω_1 and Ω_2. An analytical solution of the laminar circular Couette flow is expressed as [36]:

$$V_\theta(r) = C_1 r + \frac{C_2}{r} \tag{28}$$

with factors

$$C_1 = \frac{\Omega_2 R_2^2 - \Omega_1 R_1^2}{R_2^2 - R_1^2}, \qquad C_2 = \frac{(\Omega_1 - \Omega_2) R_1^2 R_2^2}{R_2^2 - R_1^2}. \tag{29}$$

The commercial ANSYS FLUENT software package switched to the option of the Navier–Stokes flow model and the present IB-LBM code are both employed, and the two sets of rotational flow simulation results will be compared to the analytical solution for validation purpose. For both simulations, a stationary cylinder of one-unit diameter is placed at the center of the 2D computational domain, with no-slip boundary condition strictly satisfied on the surface of the cylinder. Based on RCVM, set $\omega = 1.5$ rad/s, $r_c = 3$ units, where the peak tangent velocity (note the diameter of cylinder takes one unit), $(V_\theta)_{max}$, physically arises. Accordingly, by substituting $R_1 = 0.5$ unit, $R_2 = r_c = 3$ units, $\Omega_1 = 0$, and $\Omega_2 = \omega = 1.5$ rad/s into Eqs. (28) and (29), the analytical solution of this flow within the "ring" area becomes:

$$V_\theta(r) = \frac{\Omega_2 R_2^2}{R_2^2 - R_1^2} \cdot \frac{r^2 - R_1^2}{r} = \frac{27}{70} \cdot \frac{4r^2 - 1}{r}. \tag{30}$$

In the numerical simulations, the imposition of $(V_\theta)_{max} = r_c \omega$, which is according to RCVM, is constantly maintained at the circular line with $r = r_c$ when using FLUENT; in the present IB-LBM run, $(V_\theta)_{max}$ needs to be imposed at that circular line with $r = r_c$ only at the beginning of computation. In order to ensure the accordance with RCVM at the outer boundary of the rectangular computational domain, the local radial velocity component remains nil while the local tangential velocity component is prescribed using:

$$V_\theta = \frac{\omega r_c^2}{r} = \frac{27}{2} \cdot \frac{1}{\sqrt{x^2 + y^2}} \tag{31}$$

which is based upon Eq. (30) with $\omega = 1.5$ rad/s and $r_c = 3$ units take into consideration. Hence, the rectangular flow domain in this case can be divided into two zones: of key interest is the velocity solution within the "ring" area, which is
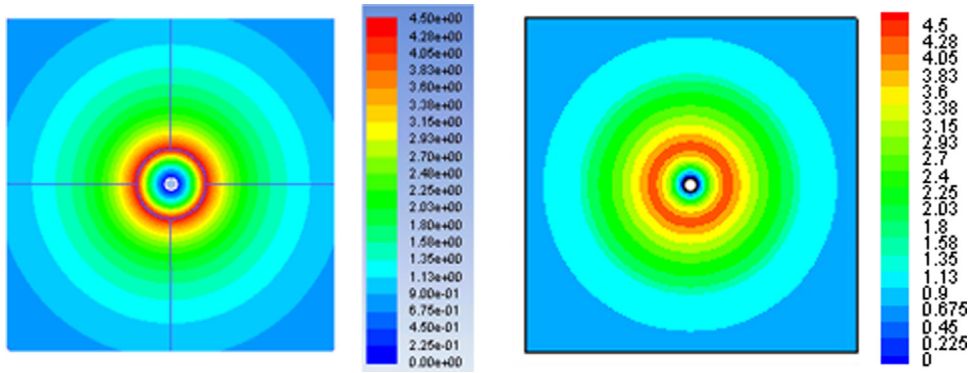
Fig. 2. Velocity magnitude contours (left: using ANSYS FLUENT; right: using LBM).
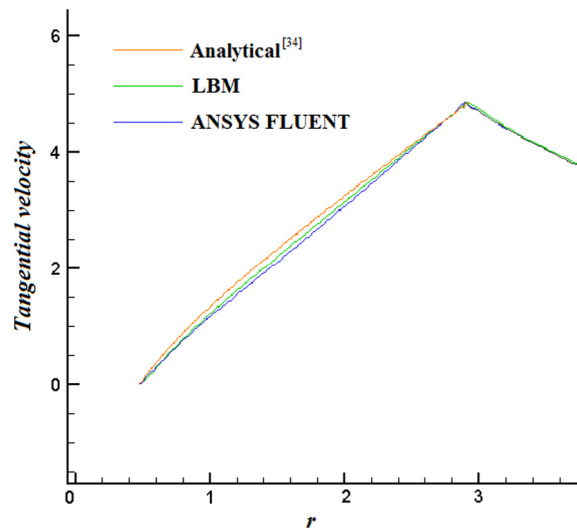

Fig. 3. Tangent velocity profile comparison.

the core zone and features the laminar circular Couette flow; the off-core zone, which is the outside of the "ring" area, is governed by the boundary condition of RCVM type and no longer within the circular Couette flow context.

The velocity magnitude contours from the two simulations are shown in Fig. 2, confirming the purely tangential flow nature of the rotational Couette flow. Detailed tangent velocity profiles along a radial line obtained by the two simulations are both depicted in Fig. 3 and compared against the available analytical solution [36]. The first range with increasing tangent velocity contains slight difference between the three solutions, the IB-LBM solution looks overall closer to the analytic solution than the N–S solution resulting from FLUENT. No visible difference between the three solutions can be detected in the second range with decreasing tangent velocity, indicating the RCVM analytic method, the present IB-LBM approach, and the Navier–Stokes flow model can converge in this off-core flow zone when the latter two employ RCVM for boundary condition use.

Remark also that neither Eq. (30) nor Eq. (31) shows the tangent velocity component has an explicit connection to the viscosity of the particular rotating fluid and, in turn, the Reynolds number of the flow. Misleadingly, this might have suggested one to think that, in a tornadic wind, the flow characteristics depend mainly on its translational flow part, V_t. At present, the tornado researchers have conventionally taken the incoming translational velocity component as characteristic velocity in determining the Reynolds number of a tornadic wind. However, both Eqs. (30) and (31) indicate that, from an analytical point of view, the angular velocity in the core zone of a tornado, Ω_2 in the Circular Couette flow formula, i.e., ω in RCVM, plays a crucial role in the magnitude of local tangent velocity component, V_θ, and in turn, the overall flow field, given that $\vec{V} = \vec{V}_t + \vec{V}_\theta$ holds in the entire tornadic wind field as indicated in Eq. (2). In fact, this angular velocity reflects the rotation intensity in a tornadic wind, β, as demonstrated in Eq. (4). In Section 5, the impact of this rotation intensity will be investigated in detail.
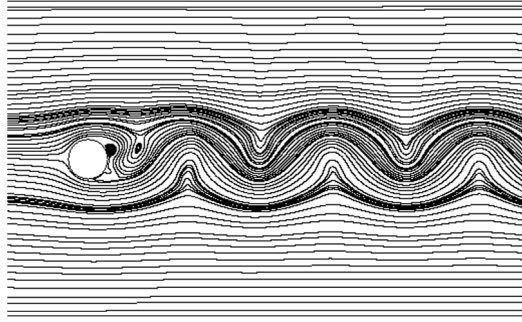
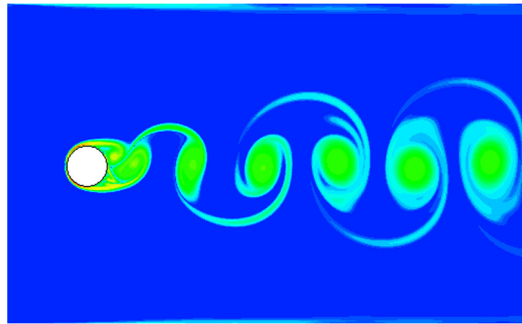**Fig. 4.** Streamlines around cylinder at $Re = 1000$.

Fig. 5. Vorticity around cylinder at $Re = 1000$.

Table 1
Comparisons of mean drag coefficient and Strouhal number at $Re = 1000$.

References	Drag coefficient	Strouhal number
Present method	1.25	0.238
COMSOL Multiphysics	1.20	0.225
J.B. Wanderley et al. [31]	0.96	0.193
S. Cao et al. [32]	1.24	0.206
Y. Lecointe et al. [33]	1.50	0.24

4.2. Translational flow at elevated Reynolds number

Now, a series of purely translational flows over a stationary cylinder at Re from 1000 to 3900 is examined here to validate the applicability of the present IB-LBM code to simulation of flows at relatively high Reynolds numbers. The computational domain occupies a $[-40, 40] \times [-12.5, 12.5]$ rectangle. The cylinder is immobile and located at the center of the rectangular domain. The mesh resolution uniformly remains $\frac{1}{50}$. This sort of test has been extensively studied using other numerical methods, and some existing results reported elsewhere will serve here as references for comparison use.

Figs. 4 and 5 illustrate the instantaneous streamlines and vorticity contours at $Re = 1000$ in the vicinity of a cylinder, respectively, and the Karman vortex street is seen in both figures. In particular, Fig. 5 clearly reveals that the vortex is shedding at a constant frequency. Here, the Strouhal number is employed to obtain the dimensionless frequency when the vortices are shed from the body:

$$St = \frac{f_q D}{V_t} \tag{32}$$

with f_q representing the vortex shedding frequency. This frequency can be acquired by examining the time evolution of, for instance, the drag coefficients. The drag and lift coefficients demonstrated in Fig. 6 look both periodically oscillating, which essentially respond to the periodic shedding of vortices from the cylinder.

A detailed comparison of the present drag coefficient and Strouhal number against other available data, as shown in Table 1, shows that the results obtained from this study are within the range of values reported in other references. Moreover, as demonstrated in Fig. 7, using the present LBM based approach, the drag coefficient ranging from $Re = 1000$ to 3900 increases monotonically and, again, agrees pretty well with the data resulting from other methods [31–33,37–39]. This indicates that present IB-LBM framework with the aid of LES can achieve reliable simulation results at elevated Reynolds
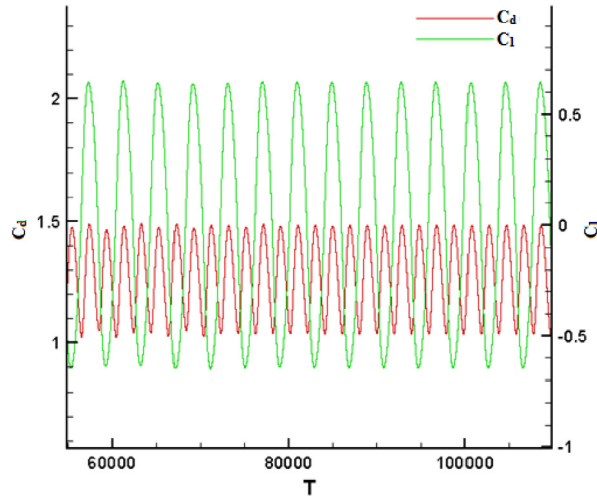
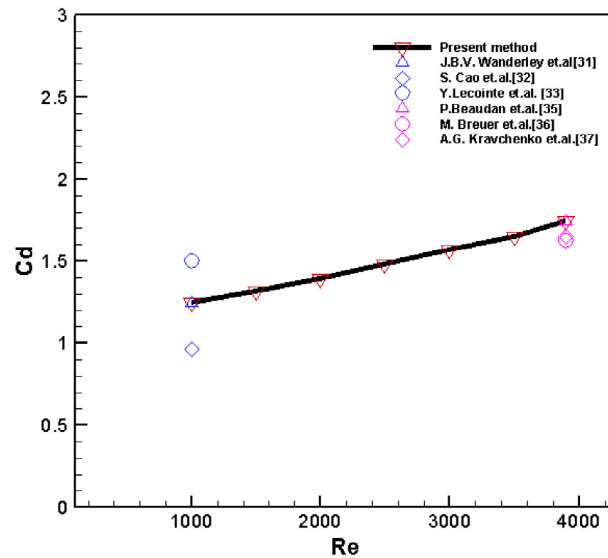**Fig. 6.** Evolution of drag and lift coefficients at $Re = 1000$.

Fig. 7. Evolution of mean drag coefficient and comparison with references.

numbers. On the other hand, this series of preliminary tests reveal that the mean drag coefficient goes up monotonically when the Reynolds number rises in this testing range while the flow is purely translational, i.e., the rotation intensity is nil ($\beta = 0$).

5. Numerical experiments

Following the validation of the present IB-LBM framework for simulation of purely rotational and translational flows in Section 4, this approach is now employed to investigate the impact of the rotation intensity in a tornado-like airflow over a construction. As described in Section 1, the scenario of a tornado passing through a building is interpreted as a superposition of a "locked" rotational airflow and a "virtual translation" of the building, which is re-tailored from the original RCVM in order to render the outer boundary condition time-independent.

In all subsequent simulations, the computational domain occupies a $[-40, 40] \times [-12.5, 12.5]$ rectangular domain. Using the re-tailored RCVM, the center of the rotational flow component is fixed at $(0, 0)$, and the initial position of the building center is located at $(35, 0)$ with a translational speed at $V_t = 0.034$ *unit/sec* towards the negative x-direction, which corresponds to a physical scenario in which the tornado is both translating in the positive x-direction and rotating while the building keeps locked and initially is 35 units away from the center of the incoming tornado.
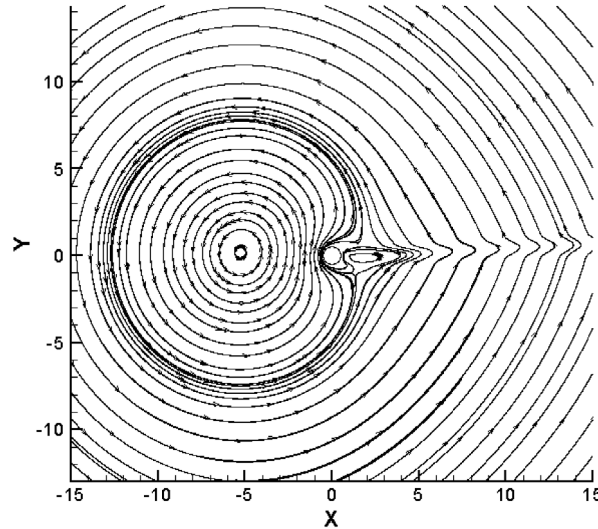
Fig. 8. Streamlines at "*core-in*" time.

Three characteristic coefficients, C_x, C_y, and C_m, which reflect the aerodynamic force components in the x- and y-directions, F_x, F_y, and the resulting moment, M, respectively, are defined as:

$$C_x = \frac{F_x}{0.5\rho V_t^2 D} \tag{33}$$

$$C_y = \frac{F_y}{0.5\rho V_t^2 D} \tag{34}$$

$$C_m = \frac{M}{0.5\rho V_t^2 (\pi D^2/4)} \tag{35}$$

and will be used for examining the wind loading on the cylindrical building with diameter D.

5.1. An example

Before focusing on the effects of the rotation intensity in a tornadic wind scenario, a case at $Re = 1000$, $r_c = 3 \ units$, and with rotation intensity specified at $\beta = 0.5$, i.e., $(V_\theta)_{max} = r_c\omega = 0.5V_t$, according to Eq. (4), is employed as example to illustrate the key aspects of numerical investigation. For the sake of description convenience, three representative time points during the tornado−building interaction are chosen for detailed observation, namely, (1) the tornado core zone reaches the building, i.e., $x_{building\_center} - x_{tornado\_center} = r_c$, which is referred to as "*core-in*" time; (2) the tornado and building centers are coinciding, i.e., $x_{building\_center} = x_{tornado\_center}$, which is referred to as "*coinciding-center*" time; and (3) the tornado core zone leaves the building, i.e., $x_{tornado\_center} - x_{building\_center} = r_c$, which is referred to as "*core-out*" time. Remark that the names of these three time points do not suggest the onset of physical phenomena in their exact sense, since the interaction between the tornadic wind and building physically takes place when $x_{building\_center} - x_{tornado\_center} > r_c$, and, also, rotation and translation are concurrent all the way in the tornado-building interaction event. Between the "*core-in*" and "*core-out*" time points in the "*primary*" stage of the tornado-building interaction, whereas before and after the primary stage are respectively referred to as "*pre-interaction*" and "*post-interaction*" stages. Figs. 8–13 depicted the streamline pattern and velocity magnitude at the three representative time points, respectively.

As demonstrated in Fig. 8, until the "*core-in*" time point, the rotational flow pattern appears overall retained except in the vicinity of the building. This indicates that, in the *pre-interaction* stage, the tornado–building interaction has not been significant yet, and the affected zone remains very restricted, mainly behind the cylinder where an eddy arises, demonstrating the dominance of the translational flow component towards the obstacle. During the *primary interaction* stage, Fig. 10 shows the tornado core area is strongly disturbed since a few eddies take place in the core zone while beyond the core zone the streamlines overall remain encircling the building. In Fig. 12, the severely disturbed flow featuring co-occurrence of a number of eddies is found in the wake region. By comparing Figs. 9, 11 and 13, the highest flow rate is found right in front of the cylinder in the *pre-interaction* stage; then, in the *primary* and *post-interaction* stages, the zone of highest flow rate is located in the wake region, and this fastest flow zone goes more distant from the building when time further elapses. Also, both Figs. 12 and 13 reveal that vortices are shedding in the wake area, suggesting the re-occurrence of the dominant translational flow component upon recalling the renowned Karman vortex street phenomenon that arises in the
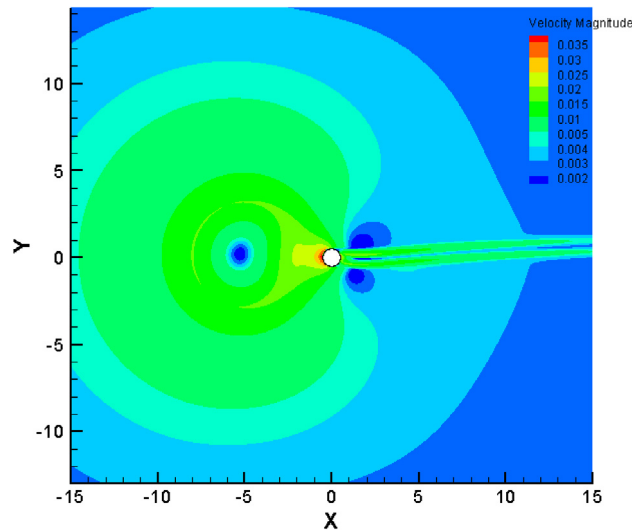
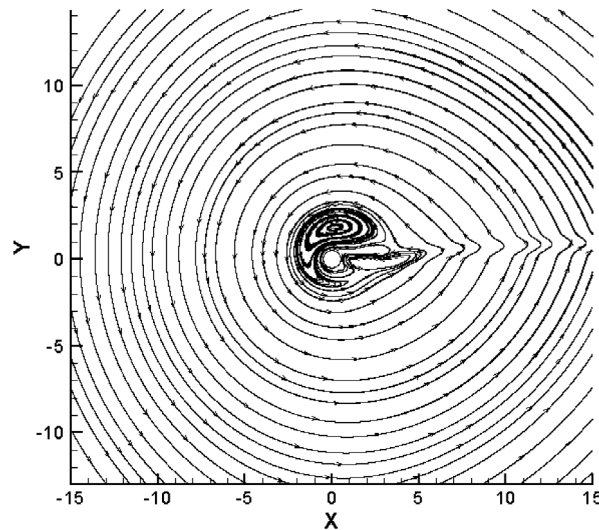**Fig. 9.** Velocity magnitude at "*core-in*" time.

Fig. 10. Streamlines at "*coinciding-center*" time.

case of a cylinder facing a purely translational incoming flow with an elevated Reynolds number. On the other hand, all these six figures exhibit a slight upward trend for the wake region, which is attributed to the counterclockwise rotational flow component in this tornadic wind. All observed characteristics echo the translation and rotation superposition nature of this flow.

Besides the qualitative analysis based on the streamline and velocity magnitude contours, quantitative analysis through evolution of C_x, C_y, and C_m, as defined in Eqs. (33)–(35), can be also made. Next, a series of tornadic flow simulations aimed at investigation of the effect of the rotation intensity will be conducted, and detailed analysis of the coming new cases will be demonstrated with the aid of the three aerodynamic coefficients.

5.2. Tornado-like wind induced loads on a cylinder

After qualitatively interpreting the overall flow features on the streamlines and velocity magnitude plottings, more details about how rotation intensity can affect the aerodynamic coefficients will be examined and discussed as follows.

Unlike in Section 4.2 where the cases examined the purely translational flows (by locking the rotation intensity at $\beta = 0$) around a single cylinder with Reynolds number ranging from 1000 to 3900 (through adjusting the fluid viscosity while
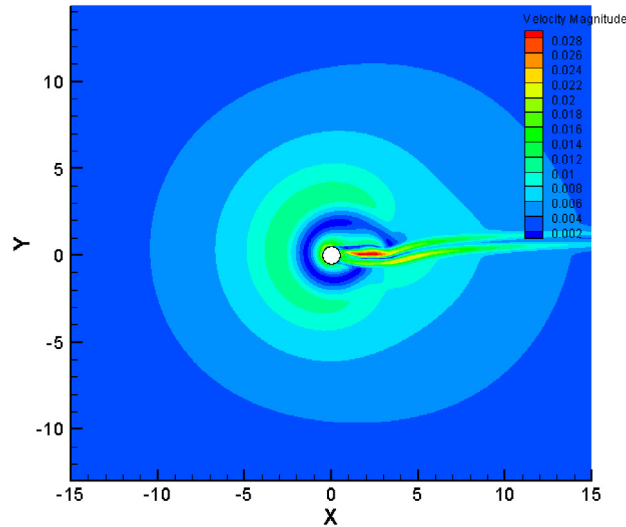
Fig. 11. Velocity magnitude at "*coinciding-center*" time.
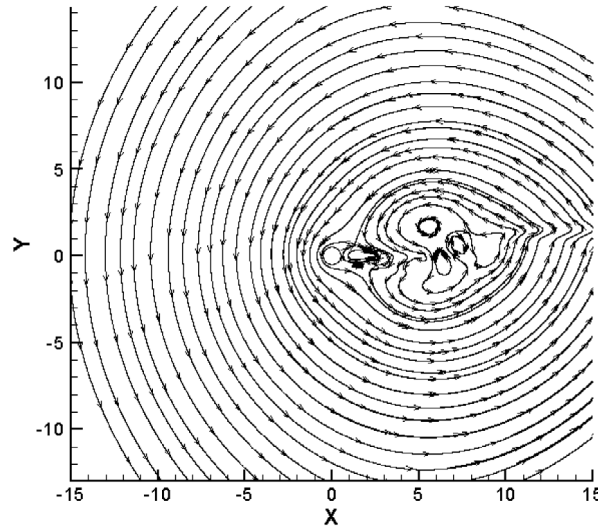

Fig. 12. Streamlines at "*core-out*" time.

fixing the characteristic velocity V_t), the tornadic wind composed of both translational and rotational flow components is the examination subject in here, and the investigation focus is now placed on the effect of rotation intensity. It was demonstrated in Section 4.2 that, in the Re range of 1000 to 3900, the "drag" coefficient, C_d, monotonically increases when Re goes up. In this section, the three aerodynamic coefficients, C_x, C_y, and C_m, are all examined for different rotation intensities, $\beta = 0.5$, 1, and 2; for each rotation intensity test series, Reynolds number starts from 1000 and then continuously increases, aiming to examine whether the wind loadings monotonically increase when Re rises.

5.2.1. *Test series 1:* $r_c\omega = 0.5V_t (\beta = 0.5)$

In this test series, $\beta = 0.5$ indicates the maximum local tangent velocity component due to the rotation component is only half of the incoming translational velocity component, hence, this flow is overall mainly dominated by the translational part. Figs. 14–16 respectively groups the evolutions of C_x, C_y, and C_m over the Re testing range from 1000 to 3900. In these three figures, the position $x = 0$ on the horizontal axis represents the time instant at which the centers of the tornado and cylinder are *nominally* coinciding if solely taking into account the translation of the tornado center; in the intervals $x < 0$ and $x > 0$, the tornado is approaching and leaving the cylinder, respectively. An overall observation of the three figures may find out two major turning points on the horizontal axis approximately located at $x = -3$ (at "*core-in*" time) and $x = 3$ (at "*core-out*" time).
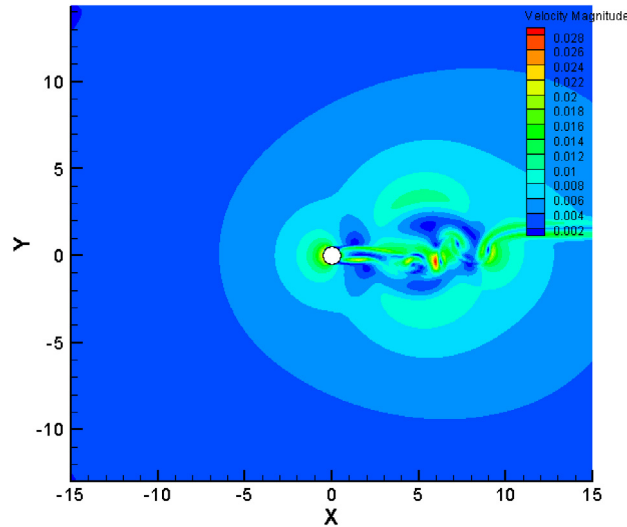
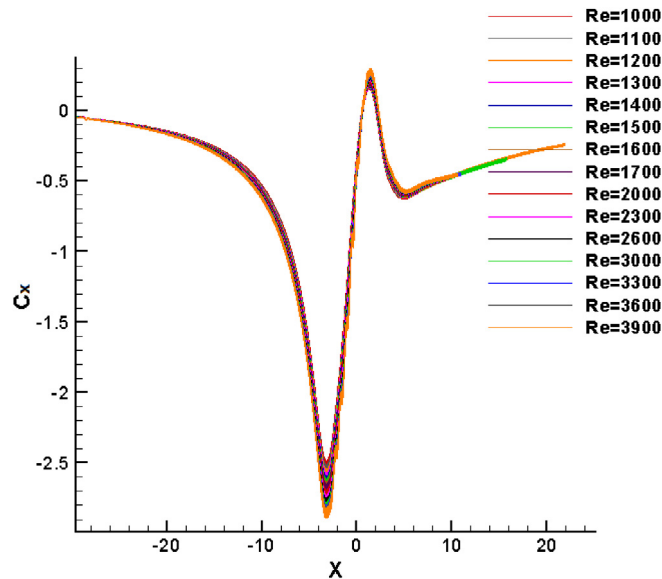**Fig. 13.** Velocity magnitude at "*core-out*" time.

Fig. 14. C_x evolutions for different Reynolds numbers at $\beta = 0.5$.

In the *pre-interaction* stage ($x < -3$), C_x and C_m decrease while C_y increases, indicating the cylinder is *pulled* towards the tornado center in the x-direction, *uplifting* in the y-direction, and *twisted* in the clockwise direction. Recall that, in this case, $\beta = 0.5$, $V_t = 0.034$ unit/s, and $r_c = 3$ units. In Figs. 14–16, when $x < -3$, the distance between the tornado center and the cylinder center, r, is greater than r_c. According to RCVM as expressed in Eq. (1), $V_\theta = r_c{}^2\omega/r = \beta V_t \frac{r_c}{r}$ when $r > r_c$. Thus, the local upward tangent velocity component (due to counterclockwise rotation in the tornadic wind) for the left half of the cylinder is larger than that for the right half, leading to a larger uplifting force exerted in the left half of the cylinder than that for the right half. This yields the overall clockwise twisting effect for this pre-interaction stage. Also, a distinct point is approximately located at $x = -10$, as the overall variation slopes for the intervals $x < -10$ and $-10 < x < -3$ are significantly different for each of Figs. 14–16, the former being smaller while the latter being larger. The steep change of the three coefficients within $-10 < x < -3$ can be interpreted again by RCVM, as the aerodynamic forces and moment are related to V_θ while, in $V_\theta = \beta V_t \frac{r_c}{r}$, β, V_t, and r_c are all constants, the slope of V_θ is proportional with $1/r^2$, which becomes more considerable with decreasing r while diminishing once $r > 10$.

The *primary interaction* stage nominally refers to the range of $-3 < x < 3$ in this case. In common, approximately at $x = -3$ ("*core-in*"time), a turning point appears for C_x, C_y, and C_m, after which C_x and C_m change to increase while C_y changes to decrease. Approximately, at $-3 < x < 0$, the right half of the tornado core moves through the cylinder, followed by the crossing of the rest left half when $0 < x < 3$. A more detailed look into Figs. 14–16 can discover that, at $x = 0$
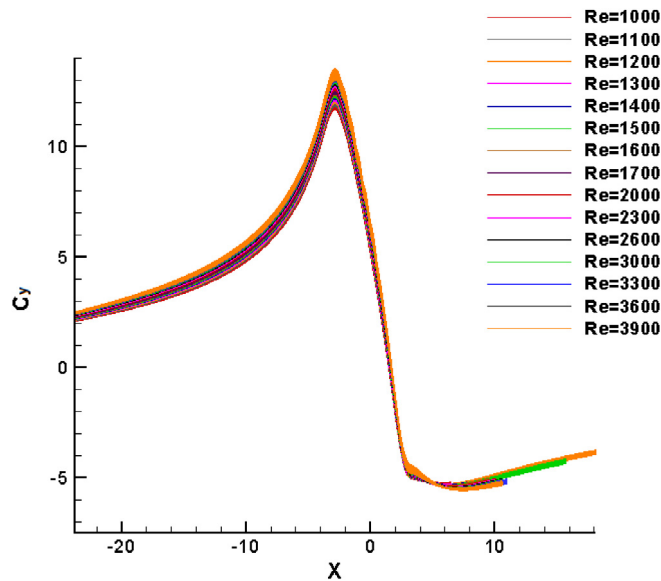
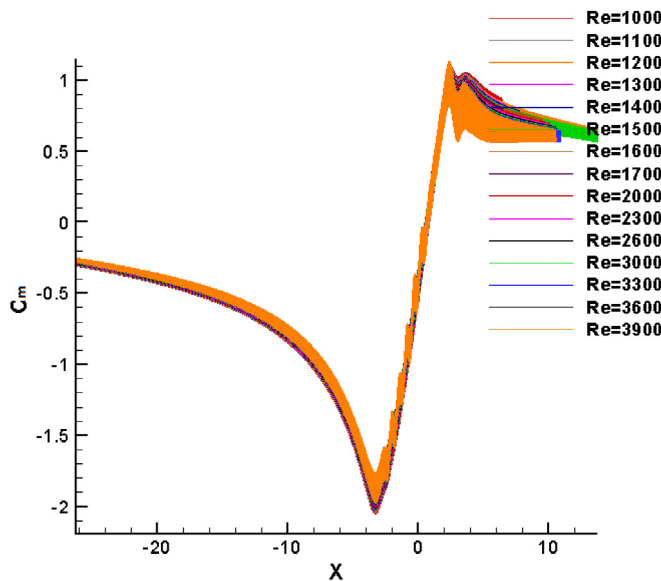**Fig. 15.** C_y evolutions for different Reynolds numbers at $\beta = 0.5$.

Fig. 16. C_m evolutions for different Reynolds numbers at $\beta = 0.5$.

(*"coinciding-center"* time at which the tornado and building centers are nominally considered coinciding), C_x, and C_m are both a bit negative while C_y is still positive. This signifies that the two centers are physically not exactly coinciding due to the concurrent rotation and translation ingredients in a tornado scenario. In Fig. 14, a second turning point is a bit before $x = 3$ (*"core-out"* time), after which C_x drops again; then, a third turning point is a bit after $x = 3$, after which C_x re-rises monotonically. The variation trend of C_m shown in Fig. 16 looks similar to C_x in Fig. 14. In Fig. 15, the second turning point for C_y to monotonically re-rise is approximately located at $x = 3$, without a third turning point detected. By recalling Figs. 12 and 13, at the *"core-out"* time, disturbance is obviously seen in the wake region after the tornado core crosses the building through the *primary* interaction stage, leaving unevenly shed vortices in the wake during the subsequent *post-interaction* stage.

Although this flow is considered mainly dominated by the translational component because of the relatively low rotation intensity ($\beta = 0.5$), the characteristics reflected by C_x, for instance, at $Re = 1000$, as included in Fig. 14, no longer contain any periodicity as shown in Fig. 6, in which a purely translational flow at $Re = 1000$ was examined. In this sense, the involvement of rotational component can radically change the flow nature regardless of the level of rotation intensity.
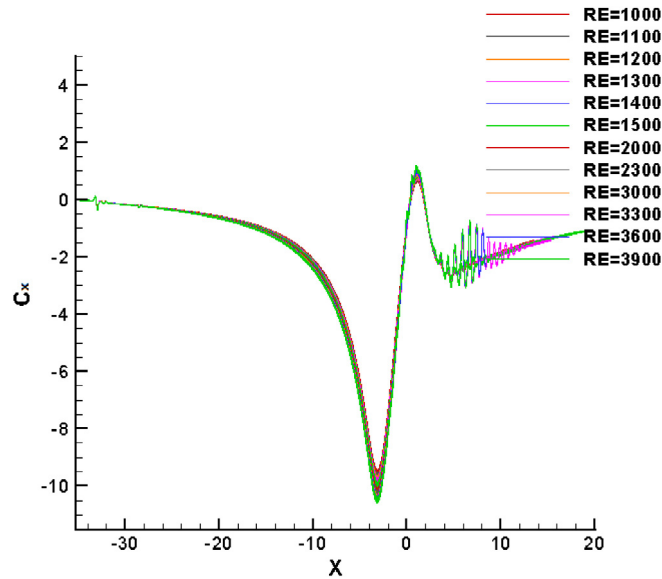
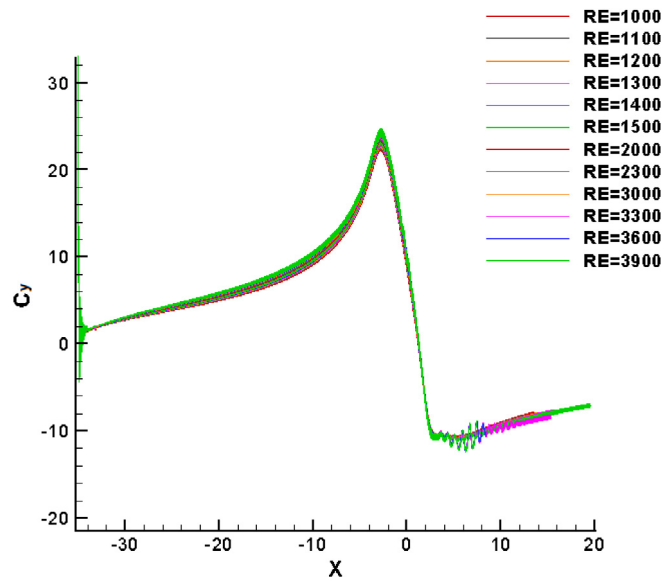**Fig. 17.** C_x evolutions for different Reynolds numbers at $\beta = 1$.

Fig. 18. C_y evolutions for different Reynolds numbers at $\beta = 1$.

In Fig. 14, if taking the extremum C_x at the *"core-in"* time as an observation subject for the "drag" coefficient, it can be noticed that, at this low rotation intensity ($\beta = 0.5$), the magnitude of this characteristic C_x keeps increasing when Re rises from 1000 to 3900 and, quantitatively, C_x goes up by about 16.5% if comparing this coefficient at $Re = 3900$ to $Re = 1000$. This increasing trend is also seen for C_d in Fig. 7 where a purely translational flow was investigated, which confirms that the translation part can overall dominate a tornadic wind at a low rotation intensity. Also, in all Figs. 14–16, a curve corresponding to a higher Reynolds number appears "thicker" than that for a lower Reynolds number. This thickness is an indication of the perturbation in the tornadic wind phenomena; the higher Reynolds number, the "thicker" curve, and the more perturbation.

5.2.2. *Test series 2:* $r_c\omega = V_t (\beta = 1)$

By doubling the angular velocity, ω, while locking all other parameters, the rotation intensity, β, gets also doubled. The curves of C_x, C_y, and C_m corresponding to $\beta = 1$ for Reynolds number ranging from 1000 to 3900 are grouped in Figs. 17–19, respectively.
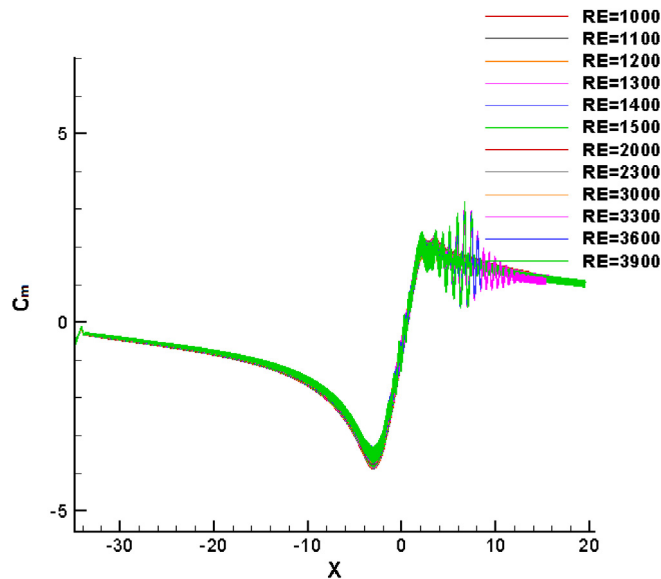
Fig. 19. C_m evolutions for different Reynolds numbers at $\beta = 1$.

The overall trends for the evolution of the three aerodynamic coefficient remain practically unchanged if compared to the case of $\beta = 0.5$ (Figs. 14–16), except that more oscillations are found in the *"post-interaction"* stage, indicating the perturbation becomes more intensive when the rotation intensity is increased. In addition, perceptible difference between the two test series arises in terms of the degree of the magnitude of wind loadings at the *"core-in"* time ($x = -3$). Using the case with $Re = 1000$ as example, C_x increases from 2.5 to 9.8 when the rotation intensity changes from 0.5 to 1.0, C_y and C_m increase nearly doubled. Clearly, the increase of rotation intensity leads to elevated tornado-like wind loadings. This is because $\beta = 1$ signifies the magnitudes of the rotational and translational velocity components are equivalent, and the x-direction stress contributed by the rotation part has become quite considerable.

In Figs. 17–19, a detailed look into the tornadic wind loadings at the *"core-in"* time reveals that the aerodynamic force and moment still monotonically increase when Reynolds number goes up. For C_x, the growth a bit exceeds 11% when Re rises from 1000 to 3900 (see Fig. 17), and this increase amount is already less than 16.5% in the case of $\beta = 0.5$.

5.2.3. **Test series 3:** $r_c\omega = 2V_t (\beta = 2)$

When the rotation intensity further increases to 2.0 and up, again, as a representative index of tornadic wind loadings, C_x at the *"core-in"* time no longer monotonically goes up with the increase of Reynolds number, as detected in Fig. 20 that depicts the case of $\beta = 2$ as an example. An enlarged view focusing on this extremum point is shown in Fig. 21, demonstrating the magnitude of C_x reaches its maximum when Re is 3000 although the upper limit of Re is 3900 in this test series.

If comparing Fig. 20 or 21 to Figs. 17 and 14, the overall wind loadings on the obstacle are found much larger than those for $\beta = 1$ or less. When looking into the cases with $Re = 3900$ but different rotation intensities ($\beta = 0.5, 1, 1.5, 2, 2.5,$ and 3), the magnitude of C_x at the *"core-in"* time is found monotonically increasing with β, as shown in Fig. 22. This suggests that, in the study of tornadic wind, the rotation intensity serves as a crucial parameter in addition to the Reynolds number that is determined conventionally using only the incoming translation velocity component as the characteristic velocity.

5.3. Critical rotation intensity

Through the test cases conducted in Section 5.2 that unfold with different rotation intensities over the same range of Reynolds number (from 1000 to 3900), the distinction appears in terms of the monotonicity of the increase of aerodynamic forces with the increase of Re. When the rotation intensity is relatively small, such as $\beta = 1$, wind loadings can be regarded as related to Reynolds number only (see, for instance, Fig. 17). When the rotation intensity rises to, for example, $\beta = 2$, the variation trend for the loadings exerted on the obstacle becomes unpredictable if still relying on Re as the sole influencing factor (see Fig. 20). Of practical interest is to locate the critical rotation intensity, beyond which the wind loadings no longer monotonically grow up with the increase of Reynolds number. An efficient way to complete this search is to use a strategy that resembles the Newton's bi-section method. That is, given the numerical results obtained in the test series with $\beta = 1$
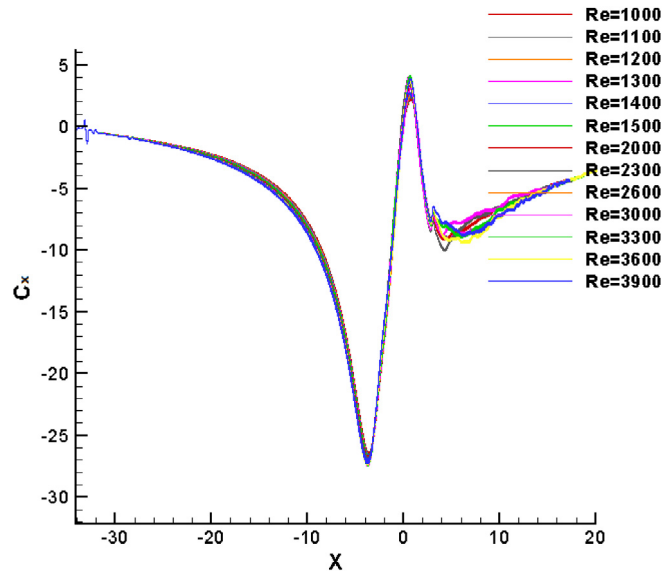
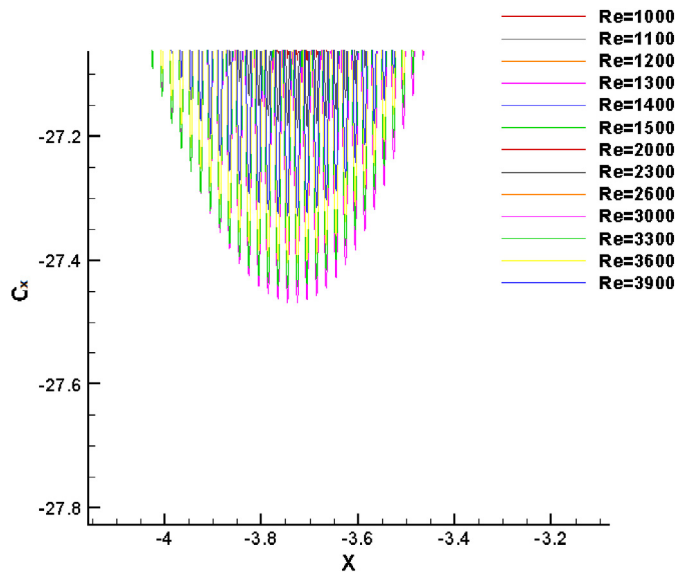**Fig. 20.** C_x evolutions for different Reynolds numbers at $\beta = 2$.

Fig. 21. C_x extrema for different Reynolds numbers at $\beta = 2$.

and $\beta = 2$, the critical rotation intensity is believed to arise in the interval [1.0, 2.0]. Then, the new testing rotation intensity is set using:

$$\beta_{new} = \frac{1}{2} \left(\beta_{mono} + \beta_{non-mono} \right) \tag{36}$$

for checking the monotonicity in question. After the monotonicity is confirmed at $\beta = 1.5$, β_{mono} is substituted by 1.5 to set a further testing rotation intensity. Employing this bi-section-like strategy, the critical rotation intensity is found to be located within the interval [1.875, 1.9375] if the interval length, $\Delta\beta = \frac{1}{16}$, is considered acceptably small. In other words, when the rotation intensity falls lower than the critical interval, the loadings on the cylinder can be viewed as relevant mainly to Reynolds number, and the loading extrema rise with the increase of Re; otherwise, no predictable relation is present between the loadings and Re. This investigation reveals that, when the rotation intensity is above its critical value, the rotational component of a tornadic wind strongly affects the overall flow characteristics, and the translational velocity component based Reynolds number becomes no longer a sole dominant factor.
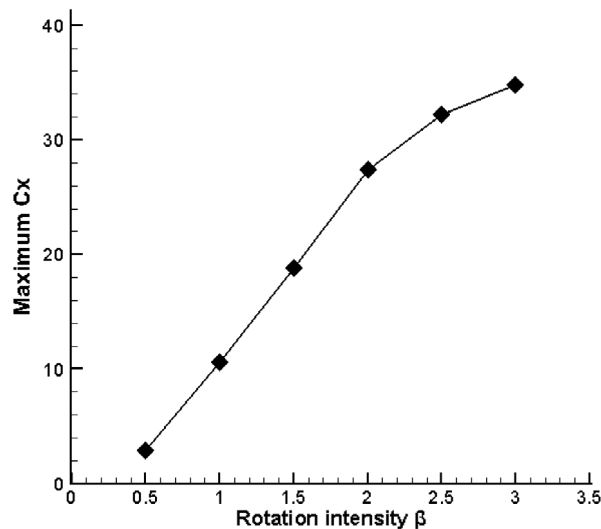
Fig. 22. Maximum C_x comparison for different β at $Re = 3900$.

6. Conclusions

In this paper, the primitive Rankine-Combined Vortex Model (RCVM) is re-tailored so that an immersed boundary (IB) lattice Boltzmann method (LBM) can be handily applied to the investigation of the tornado–construction interaction mechanism, and this hybrid framework has also been enriched by the sub-grid stress (SGS) model, so that the simulation of a tornado–building interaction scenario at an elevated Re becomes manageable with ease. The effectiveness of the present IB-LBM computational framework with the re-tailored RCVM embedded is demonstrated through the validating cases in which the IB-LBM results respectively for translational and rotational flows are found in good agreement with the simulation data obtained elsewhere using other numerical approaches.

The focus of this study is mainly placed on the new exploration of the factors that influence the characteristics of a tornadic wind. In fluid dynamics, Reynolds number is usually employed for categorizing viscous fluid flow. Particularly, when studying the tornado-like flows, the practitioners have been conventionally using the translational velocity component in RCVM as the characteristic velocity for defining the Reynolds number, and considering such a translation component based Reynolds number as a primary influencing parameter. The present study has found that the translation part based Reynolds number is of one-sided nature for identifying a tornado-like flow, since the rotation is the other part of a tornado and the change of the rotation intensity, as defined in Eq. (4), may strongly alter the tornado characteristics.

In order to evaluate the impact of the rotation intensity, the test scenario employed in this study is that a tornado-like wind passes over a cylinder. In a number of test series included in this paper, the investigation has been performed by checking, for a given rotation intensity, whether the aerodynamic coefficients monotonically rise with the increase of Reynolds number. It is found that this monotonicity holds at lower rotation intensities while disappearing at elevated rotation intensities. Then, for the purpose of capturing the critical rotation intensity that demarcates the two intervals, one being practically considered as solely dominated by Reynolds number and the other no longer manifesting that manner, a Newton's bi-section-like strategy is presented in this study, and this critical value has been detected to be within the range from 1.875 to 1.9375 in the test scenario reported in this paper.

In practice, when the rotation intensity is less than its critical value, the translational flow component can be considered dominant in the tornado dynamics, and this falls in the conventional understanding of the tornado investigation community. Many previously achieved findings in the tornado study fell into this interval, but would not necessarily apply to the other interval in which the critical rotation intensity has been exceeded. This study tends to draw more attention of tornado researchers to the tornado cases with rotation intensities greater than the critical value in spite of more challenges and complexity in this veiled tornado research branch, where the rotation part is of the same or even higher degree of significance, if compared to the translation part, and the disasters incurred are often more dreadful.

Now, this RCVM-based IB-LBM framework can investigate the tornadic wind characteristics on a horizontal x–y plane, which is of two-dimensional nature. Using conventional numerical methods, RCVM has been applied to three dimensional tornado simulations (see [13], for example, which employed the finite volume discretization). The established three-dimensional RCVM can be handily revised in the similar manner as introduced in this paper. Thus, it looks promising for the present two dimensional IB-LBM approach to be extended for three-dimensional tornado–building interaction simulation. This extension would require further algorithmic developments such that the vertical z-direction gets also pronounced. The main challenge faced by three dimensional tornadic wind field simulation lies in the aspects of programming techniques and computation facilities, demanding the enrichment of the existing IB-LBM algorithms towards parallelized three-

dimensional computations, along with the novel computing hardware, including GP-GPUs, FPGAs, for accelerating the large-scale scientific computations. These further developments aimed at three dimensional tornadic wind simulations are expected to significantly enhance the capabilities of the tornado model.

Acknowledgments

References

[1] N.B. Ward, The exploration of certain features of tornado dynamics using a laboratory model, J. Atmos. Sci. 29 (6) (1972) 1194–1204. http://dx.doi.org/10.1175/1520-0469(1972)029\protect$\relax($1194:teocfo\protect$\relax$$2.0.co;2.

[2] F.L. Haan, P.P. Sarkar, W.A. Gallus, Design, construction and performance of a large tornado simulator for wind engineering applications, Eng. Struct. 30 (4) (2008) 1146–1159. http://dx.doi.org/10.1016/j.engstruct.2007.07.010.

[3] P.H. Tari, R. Gurka, H. Hangan, Experimental investigation of tornado-like vortex dynamics with swirl ratio: the mean and turbulent flow fields, J. Wind Eng. Ind. Aerodyn. 98 (12) (2010) 936–944. http://dx.doi.org/10.1016/j.jweia.2010.10.001.

[4] H. Hu, Z. Yang, P. Sarkar, F. Haan, Characterization of the wind loads and flow fields around a gable-roof building model in tornado-like winds, Exp. Fluids 51 (3) (2011) 835–851. http://dx.doi.org/10.1007/s00348-011-1102-6.

[5] R. Rotunno, The fluid dynamics of tornadoes, Annu. Rev. Fluid Mech. 45 (1) (2013) 59–84. http://dx.doi.org/10.1146/annurev-fluid-011212-140639.

[6] T. Wilson, R. Rotunno, Numerical simulation of a laminar end-wall vortex and boundary layer, Phys. Fluids 29 (12) (1986) 3993–4005. http://dx.doi.org/10.1063/1.865740, 1958–1988.

[7] D.S. Nolan, B.F. Farrell, The structure and dynamics of tornado-like vortices, J. Atmos. Sci. 56 (16) (1999) 2908–2936. http://dx.doi.org/10.2172/782526.

[8] W. Lewellen, D. Lewellen, R. Sykes, Large-eddy simulation of a tornado's interaction with the surface, J. Atmos. Sci. 54 (5) (1997) 581–605. http://dx.doi.org/10.1175/1520-0469(1997)054<0581:lesoat>2.0.co;2.

[9] D. Lewellen, W. Lewellen, Near-surface intensification of tornado vortices, J. Atmos. Sci. 64 (7) (2007) 2176–2194. http://dx.doi.org/10.1175/jas3965.1.

[10] T. Ishihara, S. Oh, Y. Tokuyama, Numerical study on flow fields of tornado-like vortices using the les turbulence model, J. Wind Eng. Ind. Aerodyn. 99 (4) (2011) 239–248. http://dx.doi.org/10.1016/j.jweia.2011.01.014.

[11] R.P. Selvam, P.C. Millett, Computer modeling of tornado forces on buildings, Wind Struct. 6 (3) (2003) 209–220. http://dx.doi.org/10.12989/was.2003.6.3.209.

[12] S. Panneer, P.C. Millett, et al., Large eddy simulation of the tornado-structure interaction to determine structural loadings, Wind Struct. 8 (1) (2005) 49–60. http://dx.doi.org/10.12989/was.2005.8.1.049.

[13] P. Gorecki, R.P. Selvam, Rankine combined vortex interaction with a rectangular prism, Int. J. Comput. Fluid Dyn. 29 (1) (2015) 120–132. http://dx.doi.org/10.1080/10618562.2015.1010524.

[14] J. Smagorinsky, General circulation experiments with the primitive equations: I. the basic experiment*, Mon. Weather Rev. 91 (3) (1963) 99–164. http://dx.doi.org/10.1175/1520-0493(1963)091<0099:gcewtp>2.3.co;2.

[15] B. Bienkiewicz, P. Dudhia, Physical modeling of tornado-like flow and tornado effects on building loading, in: Proceeding 7th US National Conference on Wind Engineering, 1993, pp. 95–106. http://dx.doi.org/10.1115/ajkfluids2015-25815.

[16] R. Benzi, S. Succi, M. Vergassola, The lattice boltzmann equation: theory and applications, Phys. Rep. 222 (3) (1992) 145–197. http://dx.doi.org/10.1016/0370-1573(92)90090-m.

[17] S. Chen, G.D. Doolen, Lattice boltzmann method for fluid flows, Annu. Rev. Fluid Mech. 30 (1) (1998) 329–364. http://dx.doi.org/10.1146/annurev.fluid.30.1.329.

[18] C.K. Aidun, J.R. Clausen, Lattice-boltzmann method for complex flows, Annu. Rev. Fluid Mech. 42 (2010) 439–472. http://dx.doi.org/10.1146/annurev-fluid-121108-145519.

[19] C.S. Peskin, Flow patterns around heart valves: a numerical method, J. Comput. Phys. 10 (2) (1972) 252–271. http://dx.doi.org/10.1016/0021-9991(72)90065-4.

[20] C.S. Peskin, The immersed boundary method, Acta Numer. 11 (2002) 479–517. http://dx.doi.org/10.1017/cbo9780511550140.007.

[21] Z.-G. Feng, E.E. Michaelides, The immersed boundary-lattice boltzmann method for solving fluid–particles interaction problems, J. Comput. Phys. 195 (2) (2004) 602–628. http://dx.doi.org/10.1016/j.jcp.2003.10.013.

[22] Z.-G. Feng, E.E. Michaelides, Proteus: a direct forcing method in the simulations of particulate flows, J. Comput. Phys. 202 (1) (2005) 20–51. http://dx.doi.org/10.1016/j.jcp.2004.06.020.

[23] J. Wu, Y. Qiu, C. Shu, N. Zhao, X. Wang, An adaptive immersed boundary-lattice boltzmann method for simulating a flapping foil in ground effect, Comput. & Fluids 106 (2015) 171–184. http://dx.doi.org/10.1016/j.compfluid.2014.10.003.

[24] J. Wu, C. Liu, S.-C. Yang, N. Zhao, Influence of a flexible tail on the performance of a foil hovering near the ground: Numerical investigation, Eur. J. Mech. B Fluids 52 (2015) 85–96. http://dx.doi.org/10.1016/j.euromechflu.2015.02.004.

[25] F.-B. Tian, H. Luo, L. Zhu, J.C. Liao, X.-Y. Lu, An efficient immersed boundary-lattice boltzmann method for the hydrodynamic interaction of elastic filaments, J. Comput. Phys. 230 (19) (2011) 7266–7283. http://dx.doi.org/10.1016/j.jcp.2011.05.028.

[26] H. Zhang, Y. Tan, S. Shu, X. Niu, F.X. Trias, D. Yang, H. Li, Y. Sheng, Numerical investigation on the role of discrete element method in combined lbm-ibm–dem modeling, Comput. & Fluids 94 (2014) 37–48. http://dx.doi.org/10.1016/j.compfluid.2014.01.032.

[27] R. Huang, H. Wu, An immersed boundary-thermal lattice boltzmann method for solid–liquid phase change, J. Comput. Phys. 277 (2014) 305–319. http://dx.doi.org/10.1016/j.jcp.2014.08.020.

[28] D. d'Humieres, Generalized lattice-boltzmann equations, Rarefied Gas Dyn. Theory Simu. (1994) 450–458. http://dx.doi.org/10.2514/5.9781600866319.0450.0458.

[29] D. Goldstein, R. Handler, L. Sirovich, Modeling a no-slip flow boundary with an external force field, J. Comput. Phys. 105 (2) (1993) 354–366. http://dx.doi.org/10.1006/jcph.1993.1081.

[30] Z. Guo, C. Zheng, Analysis of lattice boltzmann equation for microscale gas flows: relaxation times, boundary conditions and the knudsen layer, Int. J. Comput. Fluid Dyn. 22 (7) (2008) 465–473. http://dx.doi.org/10.1080/10618560802253100.

[31] J.B. Wanderley, G.H. Souza, S.H. Sphaier, C. Levi, Vortex-induced vibration of an elastically mounted circular cylinder using an upwind tvd two-dimensional numerical scheme, Ocean Eng. 35 (14) (2008) 1533–1544. http://dx.doi.org/10.1016/j.oceaneng.2008.06.007.

[32] S. Cao, S. Ozono, Y. Tamura, Y. Ge, H. Kikugawa, Numerical simulation of reynolds number effects on velocity shear flow around a circular cylinder, J. Fluids Struct. 26 (5) (2010) 685–702. http://dx.doi.org/10.1016/j.jfluidstructs.2010.03.003.

[33] Y. Lecointe, J. Piquet, Flow structure in the wake of an oscillating cylinder, J. Fluids Eng. 111 (2) (1989) 139–148. http://dx.doi.org/10.1115/1.3243614.

[34] X. Guo, J. Yao, C. Zhong, J. Cao, A hybrid adaptive-gridding immersed-boundary lattice boltzmann method for viscous flow simulations, Appl. Math. Comput. 267 (2015) 529–553. http://dx.doi.org/10.1016/j.amc.2015.01.082.

[35] P.J. Roache, Perspective: A method for uniform reporting of grid refinement studies, J. Fluids Eng. 116 (1994) 405–413. http://dx.doi.org/10.1115/1.2910291.
[36] C. Pozrikidis, Introduction to Theoretical and Computational Fluid Dynamics, Oxford University Press, 2011.
[37] P. Beaudan, P. Moin, Numerical experiments on the flow past a circular cylinder at sub-critical reynolds number, Tech. rep., DTIC Document, 1994.
[38] M. Breuer, Numerical and modeling influences on large eddy simulations for the flow past a circular cylinder, Int. J. Heat Fluid Flow 19 (5) (1998) 512–521. http://dx.doi.org/10.1016/s0142-727x(98)10015-2.
[39] A.G. Kravchenko, P. Moin, Numerical studies of flow over a circular cylinder at red= 3900, Phys. Fluids 12 (2) (2000) 403–417. http://dx.doi.org/10.1063/1.870318, 1994-present.